Macropore flow in relation to the geometry and topology of soil macropore networks: Re-visiting the kinematic wave equation

Emilien Casali [a], Mats Larsbo [a], Johannes Koestel [a,b], Nicholas Jarvis [a,*]

[a] Department of Soil and Environment, Swedish University of Agricultural Sciences, Box 7014, 750 07 Uppsala, Sweden
[b] Soil quality and Soil Use, Agroscope, Reckenholzstrasse 191, 8046 Zürich, Switzerland

ARTICLE INFO

ABSTRACT

The rapid flow of water through soil macropores significantly affects the partitioning of precipitation between surface runoff and infiltration and also the rate of solute transport in soil, both of which have an impact on the risk of contamination of surface water and groundwater. The kinematic wave equation is often employed as a model of gravity-driven water flow through soil macropores. The exponent in this simple model influences the pore water velocity attained in the macropores at any given input rate and is usually estimated by inverse modelling against measured flow rates or water contents. In theory, the exponent in the kinematic wave equation should depend on the geometry and topology of the conducting macropore networks, although these relationships have not so far been investigated. In this study, we related metrics of soil structure derived from X-ray images to values of the kinematic exponent estimated from drainage experiments on twenty-two columns sampled at three different field sites under two contrasting land uses and at three different depths.

We found that smaller values of the exponent in the kinematic wave equation, which would equate to more rapid flow of water through soil macropores, were found in plough pan and subsoil columns of smaller macroporosity, for which biopores comprised a significant fraction. The macroporosity in these columns was more vertically oriented and poorly inter-connected, though still continuous across the sample. In contrast, topsoil columns from both arable land and grassland had better connected, denser and more isotropically-distributed macropore networks and larger values of the kinematic exponent. Our results suggest that for predictive modelling at large scales, it may be feasible to estimate the kinematic exponent using class pedotransfer functions based on pedological information such as land use and horizon type.

1. Introduction

During rainfall or irrigation, much of the water infiltrating the soil may be quickly channeled through large structural pores (e.g. root or earthworm channels, inter-aggregate pore space, fissures) that represent more or less continuous "pathways of least resistance" (Nimmo, 2021). The occurrence and strength of macropore flow depends on a complex interplay between initial and boundary conditions (e.g. rainfall intensity) and the architecture of the soil macropore networks (e.g. Jarvis et al., 2016; Gao et al., 2018; Nimmo, 2021). Macropores play an important role for soil hydrology as they improve infiltration capacity and drainage rates, thereby minimizing risks of waterlogging, surface runoff and flooding (e.g. Beven and Germann, 1982; Bronstert et al., 2023). However, the rapid non-equilibrium flow of water through soil macropores is also associated with significant ecosystem disservices,

since it may accelerate contaminant leaching to receiving water bodies (Jarvis, 2007).

The importance of macropore flow has prompted the development of many models of water flow in soil macropores (Gerke, 2006; Jarvis et al., 2016). These models vary greatly in their conceptual basis and complexity, ranging from computationally-demanding numerical solutions of the fundamental equations of water flow through the pore networks of intact soils imaged by X-ray computer tomography (e.g. Scheibe et al., 2015; Gackiewicz et al., 2022) to simple analytical solutions of these same basic equations for steady-state conditions and idealized geometries of water flow in macropores (e.g. free films of constant thickness, Germann et al., 2007; Demand and Weiler, 2021). A kinematic wave equation was first proposed by Germann (1985) as a simple and useful model of gravity-driven water flow through a soil containing macropores. This modelling approach can be interpreted as a

---

Table 1

The scaling factors with which the original image size was decreased, the range of standard deviations of the Gaussian blur filter σ for which the local tubeness of the pore space was calculated, the stepsize with which the standard deviation was changed when stepping through the σ range and a proxy for the radii of the targeted biopores extracted from the image.

Downscaling factor (–)	range of σ (vx)	σ stepsize (–)	range of targeted biopore radius (mm)
0.5	1–8	1	0.14–1.12
0.25	4–12	1	1.12–4.2
0.125	4–12	1	2.24–8.4

generalization of analytical solutions of the fundamental pore-scale flow equations that implicitly accounts for complex flow geometries in real soils, whilst encompassing the results for highly idealized flow geometries as special cases (Jarvis et al., 2017a). The exponent in this simple model reflects the geometrical configuration of water flowing through the macropores and should in principle depend on the architecture of the macropore network. However, this relationship has not been studied experimentally and is therefore still poorly understood. The aim of this study was therefore to investigate how the parameters of the kinematic wave equation are influenced by the geometry and topology of soil macropore networks. To do so, we (i) estimated the model parameter values from drainage experiments on twenty-two columns sampled from three soils at three depths (topsoil, plough pan and upper subsoil) and under contrasting land uses (arable, grassland) and (ii) investigated their relationships with various X-ray image derived metrics that quantify the architecture of the macropore networks.

2. Materials and methods

2.1. Theory

The rate of gravity-driven laminar water flow through a single "equivalent flow pathway" with limited variations in thickness can be calculated with a generalized analytical solution of Stokes law that employs the concept of the hydraulic radius r_h (m) (Childs, 1969):

$$q = \left(\frac{g}{G\mu\tau}\right)\theta r_h^2 \tag{1}$$

where q (m/s) is the flow rate, g (m s^{-2}) is the gravitational acceleration,

G (–) is a factor depending on the flow geometry that varies between 2 for cylindrical and 3 for planar geometries, μ (m^2 s^{-1}) is the kinematic viscosity, τ (–) is the flow path tortuosity (the square of the ratio of the true flow pathlength divided by the straight line distance), θ (m^3 m^{-3}) is the volumetric water content of the equivalent flow pathway and r_h is given by θ/A_w, where A_w is the wetted specific surface area in the macropore pathway. Putting appropriate values for r_h in Eq. (1) leads to special cases of this general model that are applicable to idealized flow geometries. For example, r_h takes values of $d/4$, $d/2$, and d for saturated cylindrical channels, saturated slits and free planar films, where d is the channel diameter, slit width or film width. Jarvis et al. (2017a) showed that the kinematic wave equation can be derived from Eq. (1) by assuming that A_w (m^{-1}) is a power law function of the degree of saturation:

$$\frac{A_w}{A_{max}} = \left(\frac{\theta}{\phi}\right)^\beta \tag{2}$$

where ϕ (m^3 m^{-3}) is the conducting macroporosity, A_{max} is a maximum value of the wetted specific surface area (m^{-1}) and β (–) is a parameter that reflects the geometrical configuration of water flowing in the macropores. Combining Eqs. (1) and (2) gives:

$$q = K_{s(mac)}\left(\frac{\theta}{\phi}\right)^\alpha \tag{3}$$

where the macropore saturated hydraulic conductivity $K_{s(mac)}$ is given by Kozeny's equation:

$$K_{s(mac)} = \left(\frac{g}{G\mu\tau}\right)\left(\frac{\phi^3}{A_{max}^2}\right) \tag{4}$$

and where the kinematic exponent α (-) is given by:

$$\alpha = 3 - 2\beta \tag{5}$$

For transient flow conditions, Eq. (3) must be combined with an equation of continuity:

$$\frac{\partial\theta}{\partial t} = \frac{-\partial q}{\partial z} \tag{6}$$

where t is time (s) and z is height (m). The kinematic wave model (i.e. equations (3) and (6) can be solved analytically for simple initial and
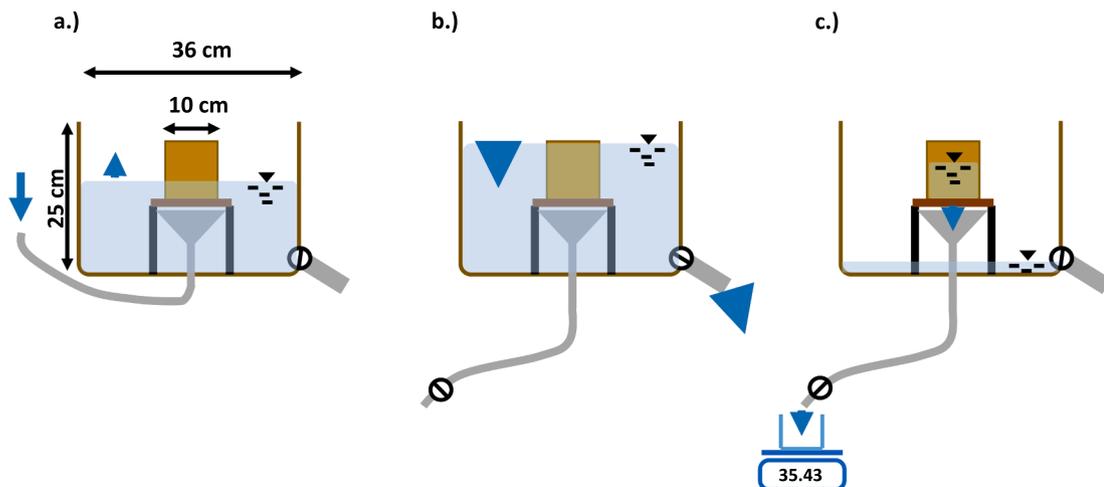

Fig. 1. Experimental setup for drainage experiments, (a) slow filling of tank from tap through bottom, (b) rapid emptying of the water outside of the sample through the side outlet, and (c) drainage of soil sample.
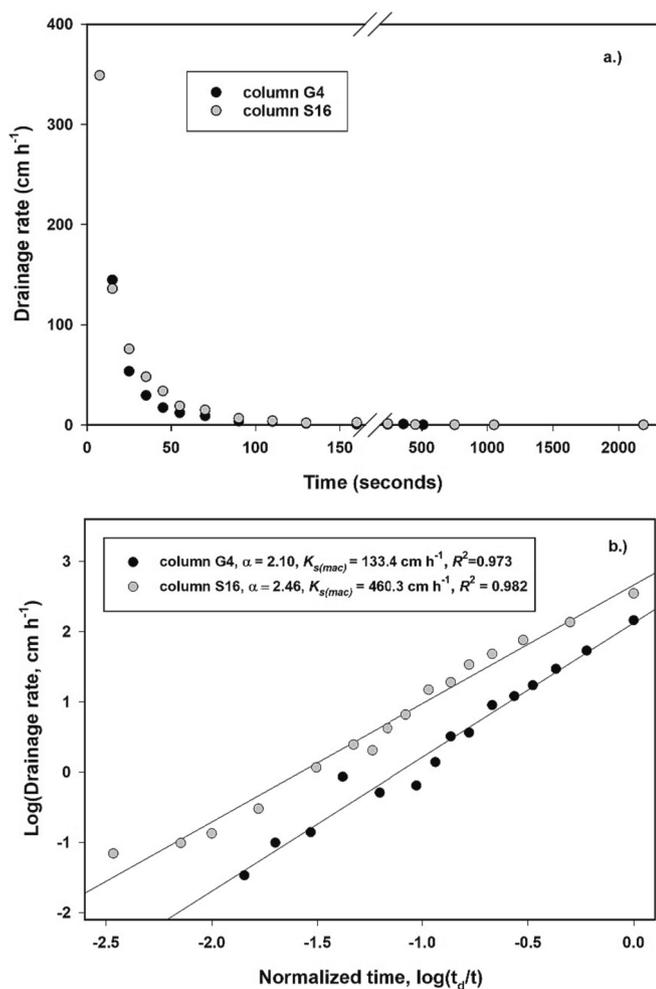
Fig. 2. Two illustrative examples of measured drainage outflow curves, plotted (a) on linear scales, and (b.) on logarithmic scales with fits of Eq. (7) to the data.
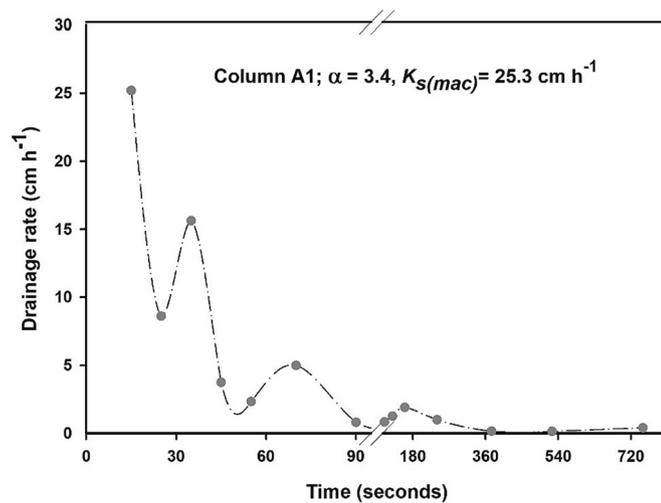

Fig. 3. Measured drainage rates for column A1 illustrating flow oscillations.

Fig. 4. Derived estimates for the parameters of the kinematic wave equation for all 22 columns (a) kinematic exponent and (b) saturated hydraulic conductivity. Means and standard deviations for each soil horizon type are shown to the right.

Larsbo et al., 2005), which has significantly widened the range of model applications, particularly for management purposes (Jarvis and Larsbo, 2012).

The kinematic exponent α, cannot be directly measured, so its value is usually inferred from measurements of water flow or water contents (e.g. Germann, 1985; Rousseau et al., 2004; Hincapié and Germann, 2009). It should take values between 1 and 3 (i.e. β should vary between zero and one) if both the wetted surface area and water velocity in the flow pathway are required to increase as both water contents and flow rates increase (Jarvis et al., 2017a). The kinematic wave equation has been shown to accurately match measured near-saturated soil water flows and water contents, usually with calibrated or fitted values of α within or rather close to this theoretical range (e.g. Rousseau et al., 2004). However, the values of $K_{s(mac)}$ needed to reproduce such measurements are orders of magnitude smaller than those predicted by Eq. (4) (e.g. Schwenk et al., 2023). This must be because at least one of the assumptions underlying the theoretical derivation of the kinematic wave equation is not satisfied in real soils. In particular, Eqs. (1)–(5) neglect the potentially important effects of pore network connectivity and constrictions on water flow rates (e.g. Childs, 1969; Berg, 2014). In this

boundary conditions (e.g. Germann, 1985) or numerically for more complex, irregular conditions (e.g. Larsbo et al., 2005). The numerical approach has been extended by combining the kinematic wave equation for macropore flow with Richards' equation for water flow in the soil matrix in a dual-permeability framework (e.g. Šimůnek, et al., 2003;
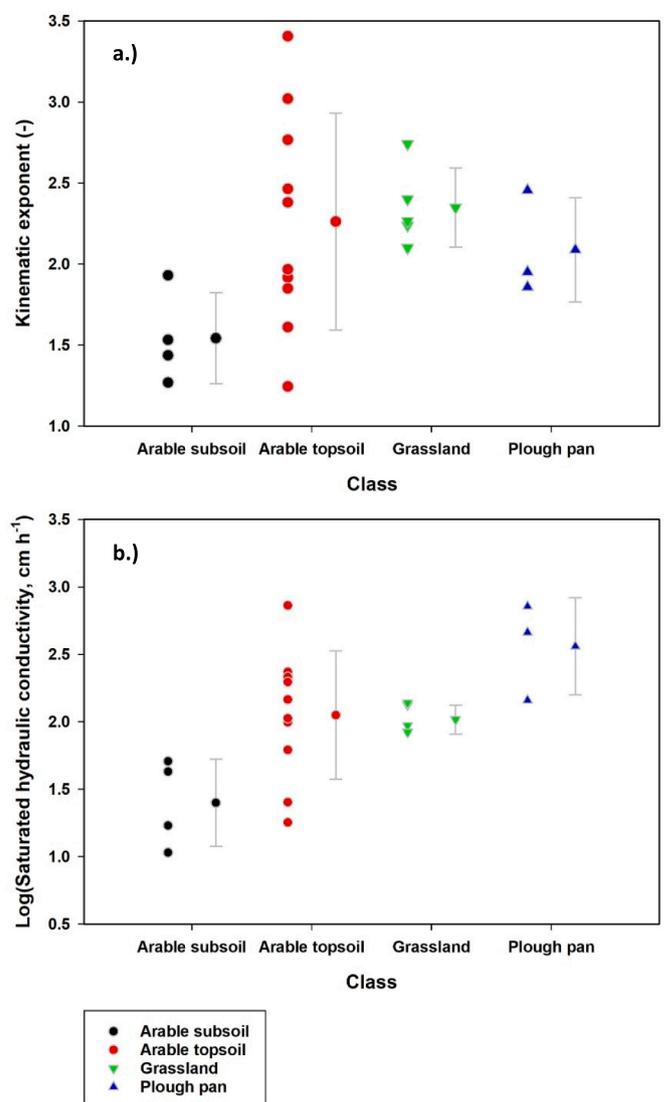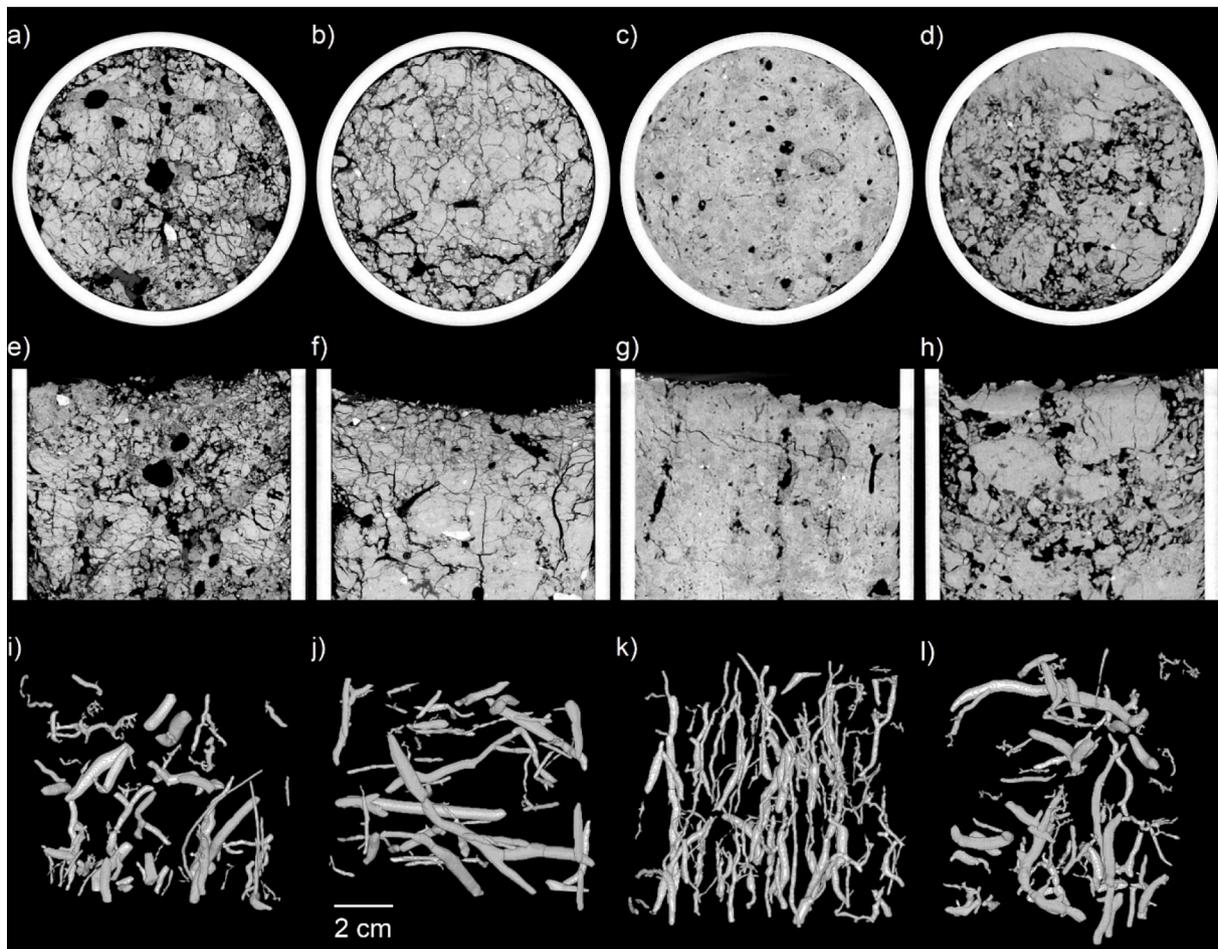
Fig. 5. Example X-ray images showing horizontal and vertical 2D slices and 3D representations of biopores in columns from grassland (G5), arable topsoil (A5), arable subsoil (S19) and plough pan (S16).

respect, X-ray studies of intact soil samples have shown that soil macroporosity consists of one or more individual networks or clusters, each comprising multiple pathways of variable thickness, including bottleneck constrictions that exert a dominant control on water flow near saturation (e.g. Koestel et al., 2018; Schlüter et al., 2020). These studies have also emphasized that the actual conducting macroporosity in Eqs. (3) and (4) should be significantly smaller than the total macroporosity due to air entrapment (Schwenk et al., 2023) as well as the presence of so-called 'dead-end' (or 'dangling') pores (Soto-Gómez et al., 2020).

2.2. Experiments

2.2.1. Soil sampling and preparation

Twenty-three aluminium soil cores (10 cm in height, 9 cm in inner diameter) were sampled from three different sites in the vicinity of Uppsala (Sweden) using a jack and anchor system, which pushes the cylinders slowly into the soil, thereby preserving the original soil structure as much as possible. Three samples (U5, U6, U10) were taken from a clay soil under arable farming at Ultuna (59º 49′ N; 17º 39′ E), nine samples (S11, S12, S13, S14, S15, S16, S18, S19, S20) from a loam-textured arable field at Säby (59º 50′ N; 17º 42′ E) and eleven samples from a clay loam in adjoining plots under permanent grassland (G1, G2, G3, G4, G5) and arable agriculture (A1, A2, A3, A4, A5, A6) at Krusenberg (59º44′ N; 17º 41′ E). Ultuna and Säby were sampled on 27th and 28th September 2017, while Krusenberg was sampled on 8th June 2022.

In an attempt to obtain samples of strongly contrasting soil structure, four of the arable soil columns were taken at approximately plough depth to represent compacted plough pans (U5, U6, S15 and S16), while

four cores were extracted from the subsoil at 30–40 cm depth (U10, S18, S19 and S20). The remaining fifteen cores were extracted from the topsoil at 0–10 cm depth, five from the permanent grassland at Krusenberg and ten from the three arable sites.

The bottom of each core was covered with a cloth secured by a rubber band. The cores were then placed in air-tight plastic bags, transported to the laboratory and stored in a cold room at 4 °C prior to the experiments. On the day before each experiment, the sample was taken out of the cold room inside its plastic bag and adjusted to room temperature for 24 h.

2.2.2. X-ray scanning and image analysis

X-ray images of each column were obtained using a GE Phoenix v|tome|x 240 industrial X-ray scanner equipped with a GE 16″flat panel detector with 2014 × 2014 detector crystals (GE DRX250RT). After some preliminary tests, we set the tube voltage to 150 kV with an electron flux of 620 µA to achieve an optimal balance between image resolution and scanning time. Beam-hardening artefacts were minimized by introducing 0.5–0.9 mm thick copper sheets into the X-ray trajectory. Each scan comprised 2000 projections with a voxel resolution of 70 µm. Radiographs were taken with an exposure time of 333 ms. The average value for the final three of a total of four radiographs was saved as the projection to minimize after-glow effects. The projections were then inverted to 16-bit 3-D grey-scale images using the GE software datos|x (version 2.1) and exported as TIFF-stacks (tagged image file format) with a 16-bit grey-scale resolution.

Image analysis was carried out using ImageJ/Fiji (Schindelin et al., 2012) with the plugins MorphoLibJ (Legland et al., 2016) and SoilJ
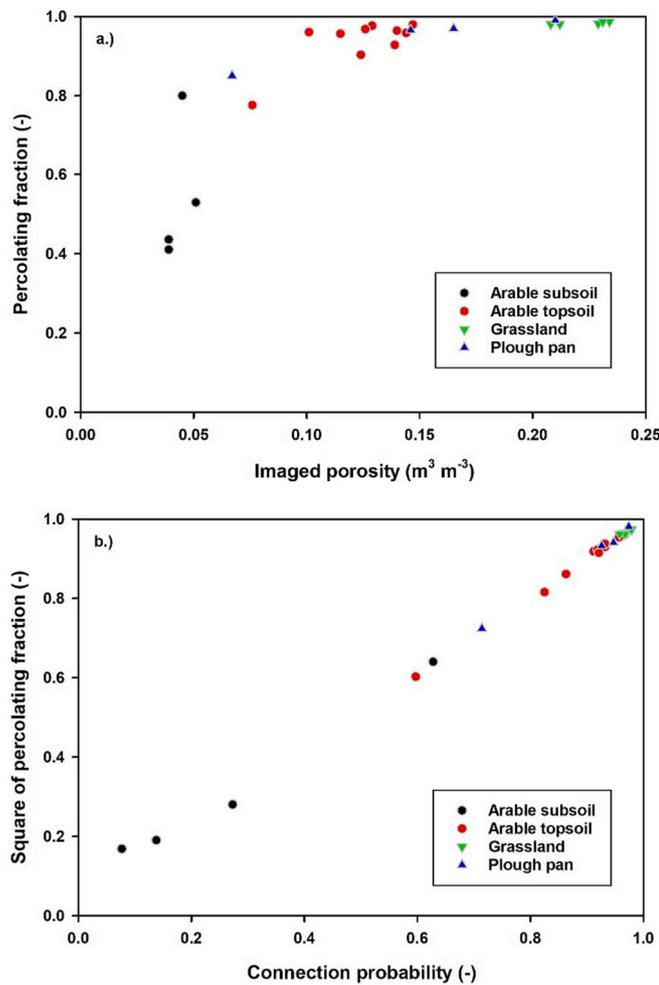
Fig. 6. Relationships between the percolating fraction of the X-ray imaged porosity and (a) the total imaged porosity and (b) the connection probability.

(Koestel, 2018). First, we reduced image noise by applying a $2 \times 2 \times 2$ median filter and sharpened the phase boundaries in the images using an unsharp mask with a standard deviation of 2 voxels and a mask weight of 0.6. Voxel layers at the top and bottom surface of the soil samples that were not entirely filled with soil were removed. We used SoilJ to automatically detect the column outlines and to rotate it into an upright position in the center of the image canvas. The grey scales of the images were then calibrated to values corresponding to air-filled macropores and the aluminium of the column walls. After analyzing the joint histogram of all X-ray images, we found that a global threshold grey scale value of 10,000 yielded good results for segmenting the air-filled pores in all 23 calibrated images.

We analyzed the imaged pore space in regions of interest (ROI) corresponding to the inner diameter of the aluminium cores (91 mm) and the full height of the imaged sample (between 70 and 90 mm). We extracted a number of metrics to quantify various aspects of the imaged pore space structure. In addition to the total imaged porosity, we obtained the fraction of this pore space comprising biopores using the method described by Lucas et al. (2022), which is an updated version of the original method outlined in Lucas et al. (2019). Briefly, we applied a tubeness filter consecutively to scaled versions of the original images with the Gaussian blur standard deviations listed in Table 1. A hysteresis thresholding with lower and upper limits of 0.55 and 0.65 was conducted on the tubeness images to segment tube-like structures. The resulting binary images were combined with a logical 'OR' operation and a distance transform watershed with Borgefors Chamfer weights was applied using MorphoLibJ. Watershedded components with a

vesselness of <0.6 were considered to be blob-like features rather than tubular pores (Frangi et al., 1998) and were therefore discarded.

We obtained the pore size distribution using the maximum inscribed sphere method. We summed the voxels within specific pore diameter ranges (<560, <1120, <2240 and < 4480 μm) and fitted a log-normal model (Kosugi, 1994) to this data to obtain the median and standard deviation of the imaged pore size distribution. Three different metrics related to pore space connectivity were quantified (Renard and Allard, 2013; Jarvis et al., 2017b; Koestel et al., 2018), the percolating porosity (i.e. the imaged pore space connected to both the top and bottom of the ROI), the connection probability (i.e. the probability that two pore voxels belong to the same cluster) and the critical pore diameter, which is defined as largest diameter sphere that can pass through the ROI from top to bottom. Finally, a simple metric of the preferred orientation of the imaged pore space (the anisotropy index, Hellner et al., 2018) was calculated by dividing the sum of intersections (i.e. boundaries between soil matrix and pore voxels) along vertical transects by the sum of intersections along two horizontal sampling transects. Sampling transects were distributed in a five by five pixel grid in the 2D plane defining the top and side boundaries of the ROI. For the horizontal direction, the average value of the two orthogonal directions was used. An isotropic pore network would result in a value close to one. Values smaller than one or larger than one indicate that pore space is preferentially vertically oriented or horizontally oriented respectively.

The X-ray analyses revealed that one of the columns from the clay soil at Ultuna (U6) had suffered from severe shrinkage during storage, with a continuous gap of several millimetres in thickness at the wall. It was therefore decided to skip further experiments on this column.

2.2.3. Drainage experiments

Each soil column was placed on a plastic support with a permeable base plate to allow the water to pass through freely. The support was placed inside a large plastic tank ($36 \times 25 \times 25$ cm) with a side opening and a bottom opening regulated by valves (Fig. 1a). Tap water was supplied from the bottom to slowly fill the tank and saturate the sample at a rate of ca. 1.5 cm^3 s^{-1}. The supply of water was stopped when the soil surface started to pond, which usually took approximately 3 h. After ca. 1 h of saturation, we quickly released the water outside of the sample through the side opening (Fig. 1b). Once this excess water had drained, we opened the valve at the base to allow water to drain from the soil column into a beaker placed on a scale (Fig. 1c). We recorded the weight of the water in the beaker on video for the first five minutes of drainage. Subsequently, the weight of water was noted manually at longer time intervals until outflow ceased, which usually took ca. 20 min. From these measurements, we constructed time series of outflow rates for each column.

Germann (1985) derived an analytical solution of the kinematic wave model (Eqs. (3) and (6)) for the initial and boundary conditions of our experiment (i.e. measurements of outflow rates during drainage of an initially saturated soil column). For a macroscopically uniform soil:

$$q = K_{s(mac)}; t < t_d$$

$$q = K_{s(mac)} \left(\frac{t_d}{t} \right)^{\left(\frac{\alpha}{\alpha-1} \right)}; t \geq t_d \qquad (7)$$

where t_d is the time (s) taken for the drainage front to reach the base of the soil column. We derived estimates of the kinematic exponent α and $K_{s(mac)}$ from ordinary linear regression of log(q) against log(t_d/t), where t_d can be estimated 'a priori' from visual inspection of the drainage plots, as the time at which the initial outflow rate starts to decrease. However, with the exception of three subsoil columns from Säby (S18, S19, S20), the drainage front moved through the column in a matter of seconds, which was much too fast for t_d to be identifiable, so the flow recession had already started at the time of the first measurement of the outflow rate. For these 20 columns, we set t_d to half of the time of the first
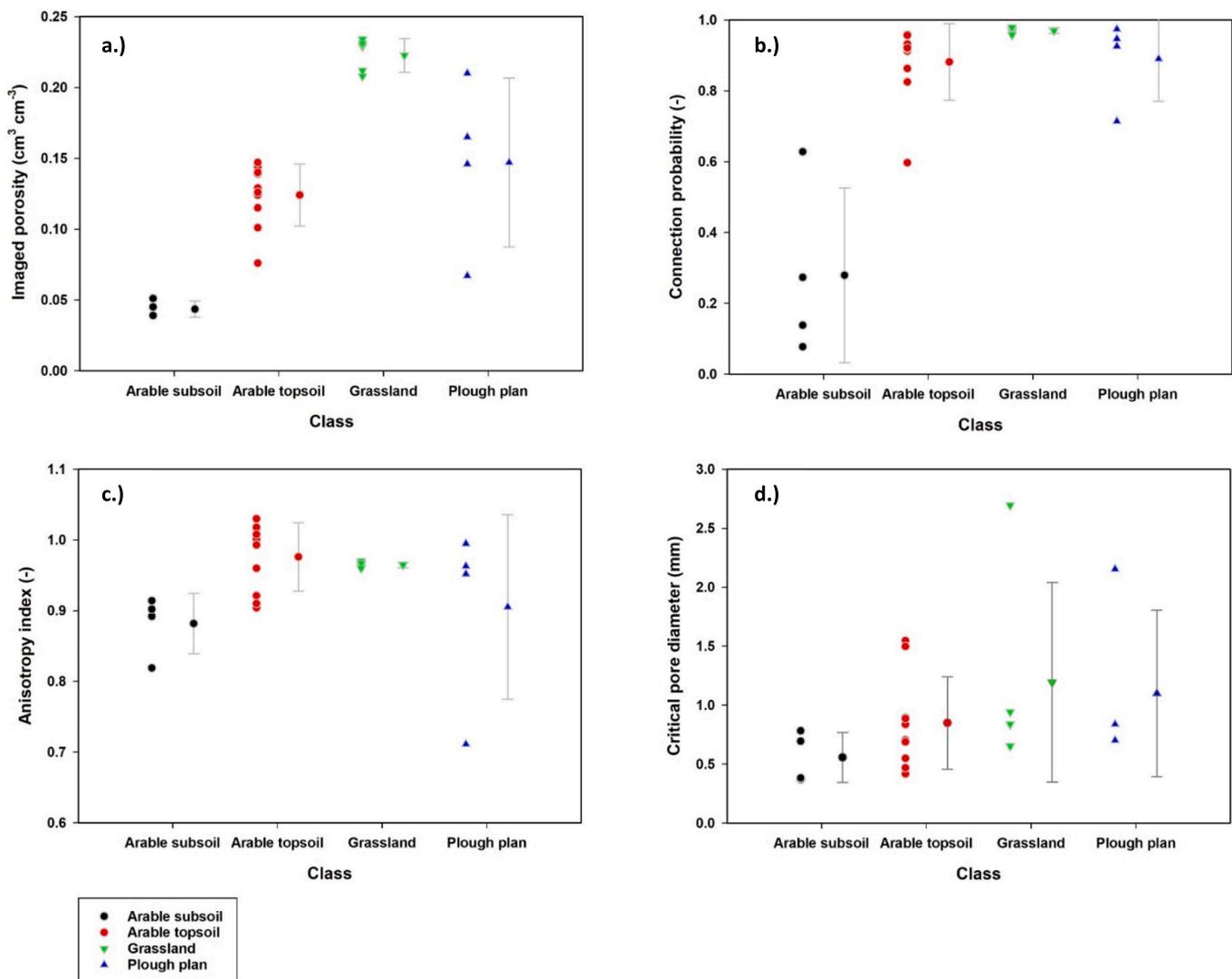
Fig. 7. Plots of (a) imaged porosity, (b) connection probability, (c) anisotropy index and (d) the critical pore diameter, grouped according to horizon type.

measurement, which was less than or equal to 25 s in all cases. It can be noted that the estimate of α was insensitive to values of t_d varying between zero and the time of the first measurement. In principle, the kinematic wave model is only appropriate for gravity-driven flow, neglecting as it does the influence of pressure potential gradients on water flow. For the conditions of our experiment, with short columns draining from saturation, deviations from a unit (gravitational) hydraulic gradient are not expected to unduly influence the results.

2.2.4. Statistical analyses

We made use of Spearman rank correlation, X-Y scatter plots and multiple linear regression to investigate inter-relationships among the soil structure parameters estimated from the X-ray images and their relationships with the parameters of the kinematic wave equation. Each sample was also classified into one of four different horizon types (arable topsoil, plough pan, arable subsoil and grassland). This was done solely to help interpretation of the results rather than to support statistical analysis, for example by one-way analysis of variance, as the sampling and classification was "ad hoc" and not systematic.

3. Results and discussion

3.1. Drainage

Eq. (7) gave excellent fits to the drainage measurements, with R^2 values greater than 0.9 for all but three columns and greater than 0.95 for 16 of the 22 columns. Fig. 2a and b shows two typical examples of the outflow measurements and the fits of Eq. (7) to the data.

In two of the columns with $R^2 < 0.9$ (S13 and A1), the outflow rates showed fluctuations (see Fig. 3 for an example). The reason for this is not clear, although it may be due to the effects of the air phase on drainage. Air must enter the soil for water to drain and it seems reasonable to suppose that narrow pore necks act as barriers to air-entry during drainage, causing 'water entrapment' (e.g. Wildenschild et al., 2001; Dunn and Silliman, 2003; Sakaki et al., 2011) and temporary reductions in outflow rates. As pressure heads decrease, trapped water is subsequently released when bottleneck pores drain, resulting in increases in drainage rates.

The derived values of the kinematic exponent largely varied within the expected range (1 < α < 3), with an overall mean value of 2.14 and a standard deviation of 0.58. Fig. 4a shows that three of the four subsoil columns had small values of α (1.26–1.53). Smaller values of α result in higher pore water velocities for a given input (i.e. precipitation rate) and thus a greater risk of preferential flow (Jarvis et al., 2017a). It can also
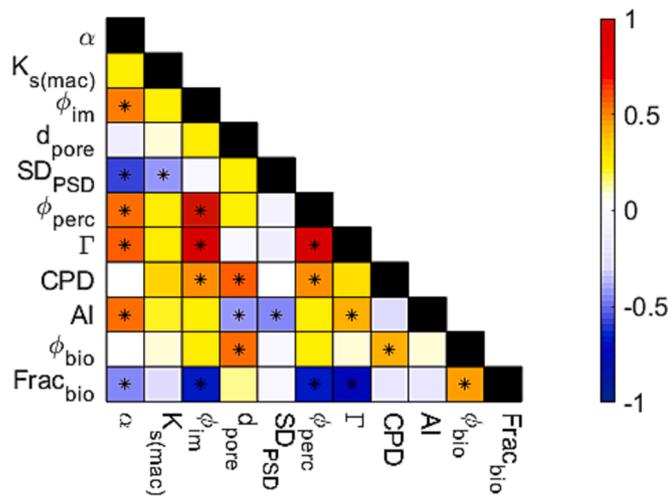
Fig. 8. Spearman correlation matrix where asterisks indicate significant (p < 0.05) correlations. α, kinematic exponent; $K_{s(mac)}$, saturated hydraulic conductivity; φ_{im}, imaged porosity; d_{pore}, median pore diameter; SD_{PSD}, standard deviation of the pore size distribution; φ_{perc}, percolating porosity; Γ, connection probability; CPD, critical pore diameter; AI, anisotropy index, φ_{bio}, bioporosity, $Frac_{bio}$, fraction bioporosity.
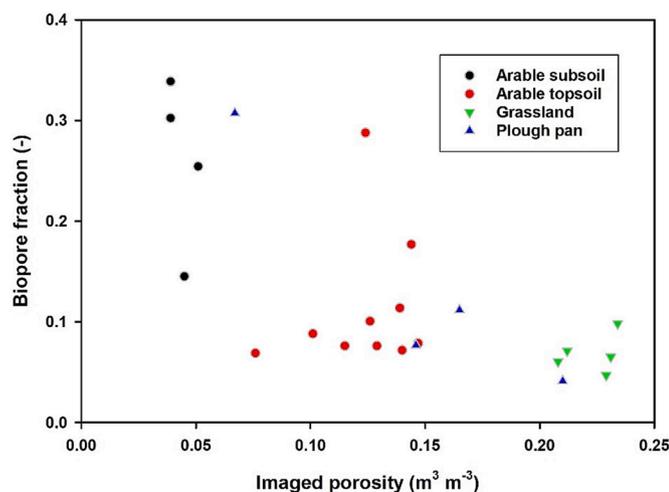

Fig. 9. The fraction of the X-ray imaged porosity classified as bio-porosity plotted against the total imaged porosity.

be noted that extreme values for the kinematic exponent shown in Fig. 4a for two arable topsoil columns (one very large, one very small) are the ones that exhibited fluctuations during drainage. The estimates of saturated hydraulic conductivity, $K_{s(mac)}$, obtained from fitting Eq. (7) to the drainage outflow curves are towards the upper end of the range of data reported in the literature (e.g. Jarvis et al., 2013) with a median value of 102.5 cm h^{-1} (Fig. 4b). As was the case for the kinematic exponent, the subsoil columns had among the smallest values of $K_{s(mac)}$.

3.2. Soil structure

Fig. 5 shows 2D vertical and horizontal slices of the X-ray images of four of the columns, representing typical samples for each of the four groups, as an illustration of the contrasting soil structures they exhibit. 3-D representations of the biopore networks in each column are also shown. The grassland column from the topsoil at Krusenberg (G5) has a well-developed fine aggregate structure and many cylindrical biopores, although these do not appear to be vertically continuous across the sample. The topsoil column taken from the adjoining arable plot at

Krusenberg (A5) is also characterized by some disconnected biopores and a strong aggregated structure, although this appears to be much coarser than in the grassland. The subsoil sample from Säby (S19) has a dense matrix with large and continuous biopores that are also predominantly oriented in the vertical direction. The plough pan from the clay soil at Säby (S16) has a dense matrix with some large clods interspersed with much finer aggregates as well as some large, more amorphous and less vertically oriented biopores.

According to the Young-Laplace equation, only pores larger than ca. 600 μm in diameter at the centre of the column would have drained by the end of the experiment. However, Fig. S1 shows that the imaged pore space larger than 560 μm in diameter is strongly correlated with the total X-ray imaged porosity ($r^2 = 0.97$, p < 0.0001) and comprises ca. 80% of the total. In the following, we assume that the metrics of soil structure derived for the total imaged pore space are also relevant for the portion of the pore network that drained.

The log-normal model fitted the imaged pore size distributions very well in all cases (see Fig. S2 in the supplementary information). These results lend further support to the use of log-normal functions to describe soil water retention in the macropore region in dual-porosity models (e.g. Romano et al., 2011; Klöffel et al., 2022). The estimated values of median pore diameter and standard deviation for each class of soil horizon are shown in Fig. S3.

All of the columns had imaged pore networks that percolated (i.e. they were continuous from top to bottom). Fig. 6a shows that our data supports the results of previous studies in that soil macropore networks follow concepts from percolation theory, such that the percolating fraction depends on the macroporosity, with a steep increase above a percolation threshold of a few percent (e.g. Jarvis et al., 2017b; Koestel et al., 2018; Schlüter et al., 2018, 2020; Lucas et al., 2020). The 1:1 relationship between the square of the percolating fraction and the connection probability shown in Fig. 6b indicates that these connectivity metrics are interchangeable for most of the columns, reflecting the presence of a single dominant percolating network at large macroporosities well above the percolation threshold (Jarvis et al., 2017b). Three of the four arable subsoil columns are exceptions, since they have more disconnected macropore networks that are closer to the percolation threshold (Fig. 6a and b).

The two remaining quantitative metrics of soil structure, the critical pore diameter and the anisotropy index, are shown in Fig. 7, along with the imaged porosity and the connection probability. Fig. 7a and b confirms that the grassland columns are characterized by large macroporosities (>0.2 m^3 m^{-3}) in well-connected networks, while the macroporosity in the arable subsoil columns is ca. 4–5 times smaller and much less well connected. Fig. 7c also shows that whereas the macroporosity in the grassland and arable topsoil columns is distributed more or less isotropically, it appears to be somewhat more vertically oriented in the four arable subsoil columns, as well as in one of the plough pan samples. Compared with previous values reported in the literature (e.g. Koestel et al., 2018), the values of critical ('bottleneck') pore diameter measured in this study were generally large (see Fig. 7d), with an overall mean value of 0.92 mm and a standard deviation of 0.56 mm. Taken together with Fig. 6a, Fig. 7d shows that all of the soil columns contained large diameter macropores that were continuous from the top to the bottom.

Fig. 8 shows correlations among the metrics of soil structure. This suggests that some of the differences among horizon types illustrated in Fig. 7b–d may be attributed to the origins of the macroporosity. In particular, cylindrically-shaped macropores that are presumed to be of biological origin are on average larger, less well inter-connected and have fewer bottleneck flow constrictions. Fig. 9 shows that these biopores comprise a much larger fraction of the macroporosity in three of the four subsoil columns and one of the plough pan columns.
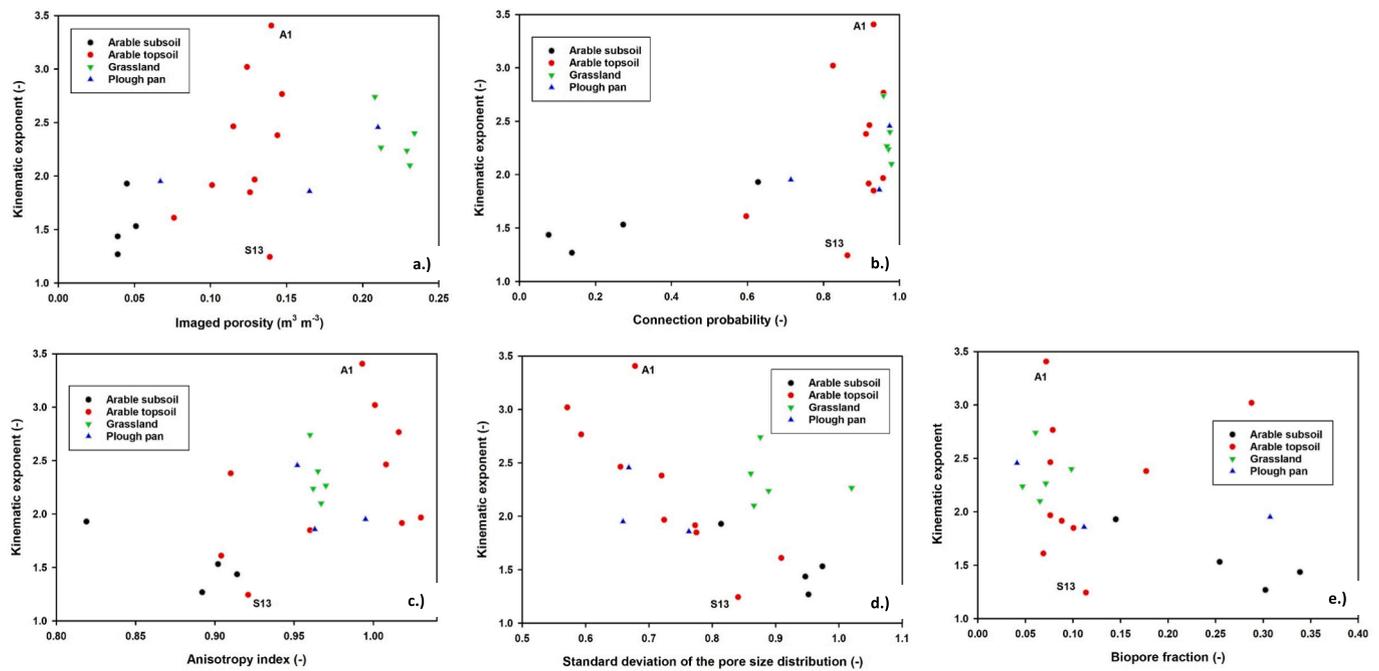
Fig. 10. The kinematic exponent plotted against (a) X-ray imaged porosity, (b) connection probability, (c) anisotropy index, (d) standard deviation of the pore size distribution, and (e) the biopore fraction.

3.3. How does soil structure influence the parameters of the kinematic wave equation?

Fig. 8 shows that with the exception of the standard deviation of the pore size distribution, SD_{PSD}, the variations in saturated hydraulic conductivity cannot be explained by any of the X-ray imaged structure parameters. The correlation of $K_{s(mac)}$ with SD_{PSD} (Fig. 8) is not easy to explain at first sight. However, it may be due to collinearity as SD_{PSD} is also correlated strongly with the macroporosity in the largest diameter class (>4480 μm; $R = 0.68$, $p = 0.0005$). Weak positive relationships between $K_{s(mac)}$ and both the percolating porosity and the critical pore diameter can also be discerned (Fig. S4), although these are not significant at $p = 0.05$, which may be partly due to the small number of investigated samples and thus lack of statistical power as well as the influence of outlier data. Nevertheless, it seems reasonable to suppose that the comparatively large values of $K_{s(mac)}$ found in our study (Fig. 4b) can be explained by the large percolating macroporosities and a lack of severe flow constrictions in the pore space of all columns (Fig. 7d; see also Koestel et al., 2018; Schlüter et al., 2020).

In contrast, the kinematic exponent α is significantly correlated to several of the metrics of soil structure, including X-ray imaged porosity, the biopore fraction, the anisotropy index, the standard deviation of the pore size distribution and two measures of connectivity, the percolating porosity and the connection probability (Fig. 8). As explained above and shown in Figs. 6 and 8, the percolating porosity and the connection probability are almost perfectly correlated and both are controlled by the imaged porosity. Fig. 10a–e suggest that correlations between the kinematic exponent and metrics of soil structure would be even stronger if the data for the two columns which exhibited oscillatory flow behaviour (A1 and S13) were removed. The negative correlation of α with SD_{PSD} (Fig. 8; Fig. 10d) may be due to collinearity since, as noted earlier, SD_{PSD} is correlated strongly with the macroporosity in the largest diameter class (>4480 μm) as well as with the anisotropy index (Fig. 8).

We attempted to derive equations to explain variations in the parameters of the kinematic wave equation from X-ray metrics using multiple linear regression. However, this approach failed because of the very strong collinearity among the predictor variables (Fig. 8) and the small number of samples. It should be noted that although such an

equation might have helped us to interpret the data, it would not be of much use as a way to estimate the kinematic exponent in predictive modelling applications. This is because, in principle, pedotransfer functions should rely on easily-measured soil properties to estimate model parameters that are more difficult to measure. In this context, it is arguably just as easy and quick to derive the kinematic exponent from flow measurements as it is to quantify soil structure by X-ray.

4. Conclusions

Smaller values of the exponent in the kinematic wave equation, α, which would equate to more rapid preferential flow of water through soil macropore networks, were found in soil columns of smaller macroporosity comprising pore networks that are less well connected, although still continuous through the column, and containing large more vertically oriented macropores. With such a pore network architecture, the water held in the macropores could drain rapidly from saturation. In these columns, which were sampled from the upper subsoil of arable land and, in one case, from a plough pan, macropores of biological origin constituted ca. 25–30% of the total X-ray imaged porosity. In contrast, topsoil samples from both arable land and grassland tended to have larger values of the kinematic exponent. In these columns, biopores comprised a smaller proportion of the imaged macroporosity and the macropore networks were better connected, denser and distributed more isotropically. Thus, although more research is clearly needed, our results suggest that for predictive flow and transport modelling at large scales, it may be feasible to estimate the kinematic exponent using class pedotransfer functions based on pedological information such as land use and horizon type.

Data statement

The complete data set can be found in the EXCEL file *Casali et al data file.xlsx* in the supplementary information.

CRediT authorship contribution statement

Emilien Casali: Methodology, Formal analysis, Investigation, Writing – original draft. **Mats Larsbo:** Conceptualization, Methodology, Formal analysis, Supervision, Writing – review & editing, Funding

acquisition. **Johannes Koestel:** Conceptualization, Methodology, Formal analysis, Supervision, Writing – review & editing, Funding acquisition. **Nicholas Jarvis:** Conceptualization, Methodology, Supervision, Writing – review & editing, Project administration, Funding acquisition.

Declaration of Competing Interest

The authors declare that they have no known competing financial interests or personal relationships that could have appeared to influence the work reported in this paper.

Data availability

Data will be made available on request.

Appendix A. Supplementary data

Supplementary data to this article can be found online at https://doi.org/10.1016/j.jhydrol.2024.130732.

References

Berg, C., 2014. Permeability description by characteristic length, tortuosity, constriction and porosity. Transp. Porous Media 103, 381–400.

Beven, K., Germann, P., 1982. Macropores and water flow in soils. Water Resour. Res. 18, 1311–1325.

Bronstert, A., Niehoff, D., Schiffler, G., 2023. Modelling infiltration and infiltration excess: the importance of fast and local processes. Hydrol. Process. 37, e14875.

Childs, E., 1969. An Introduction to the Physical Basis of Soil Water Phenomena. J. Wiley & Sons Ltd., London, p. 493.

Demand, D., Weiler, M., 2021. Potential of a gravity-driven film flow model to predict infiltration in a catchment for diverse soil and land cover combinations. Water Resour. Res. 57.

Dunn, A., Silliman, S., 2003. Air and water entrapment in the vicinity of the water table. Groundwater 41, 729–734.

Frangi, A., Niessen, W., Vincken, K., Viergever, M., 1998. Multiscale vessel enhancement filtering. In Medical Image Computing and Computer-Assisted Intervention — MICCAI'98. Springer, Berlin Heidelberg, pp. 130–137.

Gackiewicz, B., Lamorski, K., Kochiieru, M., Sławiński, C., Hsu, S.-Y., Chang, L.-C., 2022. Hybrid modelling of saturated water flow in percolating and non-percolating macroporous soil media. Geoderma 406, 115467.

Gao, M., Li, H.-Y., Liu, D., Tang, J., Chen, X., Chen, X., Blöschl, G., Leung, L., 2018. Identifying the dominant controls on macropore flow velocities in soils: a meta-analysis. J. Hydrol. 567, 590–604.

Gerke, H., 2006. Preferential flow descriptions for structured soils. J. Plant Nutr. Soil Sci. 169, 382–400.

Germann, P., 1985. Kinematic wave approach to infiltration and drainage into and from soil macropores. Trans. Am. Soc. Agric. Eng. 28, 745–749.

Germann, P., Helbling, A., Vadilonga, T., 2007. Rivulet approach to rates of preferential infiltration. Vadose Zone J. 6, 207–220. https://doi.org/10.2136/vzj2006.0115.

Hellner, Q., Koestel, J., Ulén, B., Larsbo, M., 2018. Effects of tillage and liming on macropore networks derived from X-ray tomography images of a silty clay soil. Soil Use Manag. 34, 197–205.

Hincapié, I., Germann, P., 2009. Impact of initial and boundary conditions on preferential flow. J. Contam. Hydrol. 104, 67–73.

Jarvis, N., 2007. Review of non-equilibrium water flow and solute transport in soil macropores: principles, controlling factors and consequences for water quality. Eur. J. Soil Sci. 58, 523–546.

Jarvis, N., Koestel, J., Messing, I., Moeys, J., Lindahl, A., 2013. Influence of soil, land use and climatic factors on the hydraulic conductivity of soil. Hydrol. Earth Syst. Sci. 17, 5185–5195.

Jarvis, N., Koestel, J., Larsbo, M., 2016. Understanding preferential flow in the vadose zone: recent advances and future prospects. Vadose Zone J. https://doi.org/10.2136/vzj2016.

Jarvis, N., Larsbo, M., 2012. MACRO (V5.2): Model use, calibration and validation. Trans. Am. Soc. Agricult. Biol. Eng. 55, 1413–1423.

Jarvis, N., Koestel, J., Larsbo, M., 2017a. Reply to 'Comment on "Understanding preferential flow in the vadose zone: recent advances and future prospects" by N. Jarvis et al'. Vadose Zone J. 16.

Jarvis, N., Larsbo, M., Koestel, J., 2017b. Connectivity and percolation of structural pore networks in a cultivated silt loam soil quantified by X-ray tomography. Geoderma 287, 71–79.

Klöffel, T., Jarvis, N., Yoon, S.-W., Barron, J., Giménez, D., 2022. Relative entropy as an index of soil structure. Eur. J. Soil Sci. 73.

Koestel, J., 2018. SoilJ: an Imagej plugin for the semiautomatic processing of three-dimensional X-ray images of soils. Vadose Zone J. 17 (1), 1–7.

Koestel, J., Dathe, A., Skaggs, T., Klakegg, O., Ahmad, M.A., Babko, M., Giménez, D., Farkas, S., Nemes, A., Jarvis, N., 2018. Estimating the permeability of naturally structured soil from percolation theory and pore space characteristics imaged by X-ray. Water Resour. Res. 54.

Kosugi, K., 1994. Three-parameter lognormal distribution model for soil water retention. Water Resour. Res. 30, 891–901.

Larsbo, M., Roulier, S., Stenemo, F., Kasteel, R., Jarvis, N., 2005. An improved dual-permeability model of water flow and solute transport in the vadose zone. Vadose Zone J. 4, 398–406.

Legland, D., Arganda-Carreras, I., Andrey, P., 2016. MorphoLibJ: integrated library and plugins for mathematical morphology with ImageJ. Bioinformatics 32, btw413–btw3534. https://doi.org/10.1093/bioinformatics/btw413.

Lucas, M., Schlüter, S., Vogel, H.-J., Vetterlein, D., 2019. Soil structure formation along an agricultural chronosequence. Geoderma 350, 61–72.

Lucas, M., Vetterlein, D., Vogel, H.-J., Schlüter, S., 2020. Revealing pore connectivity across scales and resolutions with X-ray CT. Eur. J. Soil Sci. 72, 546–560.

Lucas, M., Nguyen, L., Guber, A., Kravchenko, A., 2022. Cover crop influence on pore size distribution and biopore dynamics: enumerating root and soil faunal effects. Front. Plant Sci. 13.

Nimmo, J., 2021. The processes of preferential flow in the unsaturated zone. Soil Sci. Soc. Am. J. 85, 1–27.

Renard, P., Allard, D., 2013. Connectivity metrics for subsurface flow and transport. Adv. Water Resour. 51, 168–196.

Romano, N., Nasta, P., Severino, G., Hopmans, J., 2011. Using bimodal lognormal functions to describe soil hydraulic properties. Soil Sci. Soc. Am. J. 75, 468–480.

Rousseau, M., Ruy, S., Di Pietro, L., Angulo-Jaramillo, R., 2004. Unsaturated hydraulic conductivity of structured soils from a kinematic wave approach. J. Hydraul. Res. 42 (S1), 83–91.

Sakaki, T., Limsuwat, A., Illangasekare, T., 2011. An improved air pressure measuring method and demonstrated application to drainage in heterogeneous soils. Vadose Zone J. 10, 706–715.

Scheibe, T.D., Perkins, W.A., Richmond, M.C., McKinley, M.I., Romero-Gomez, P.D.J., Oostrom, M., Wietsma, T.W., Serkowski, J.A., Zachara, J.M., 2015. Pore-scale and multiscale numerical simulation of flow and transport in a laboratory-scale column. Water Resour. Res. 51 (2), 1023–1035.

Schindelin, J., Arganda-Carreras, I., Frise, E., Kaynig, V., Longair, M., Pietzsch, T., Preibisch, S., Rueden, C., Saalfeld, S., Schmid, B., Tinevez, J.Y., White, D.J., Hartenstein, V., Eliceiri, K., Tomancak, P., Cardona, A., 2012. Fiji: an open-source platform for biological-image analysis. Nat. Methods 9 (7), 676–682.

Schlüter, S., Großmann, C., Diel, J., Wu, G.-M., Tischer, S., Deubel, A., Rücknagel, J., 2018. Long-term effects of conventional and reduced tillage on soil structure, soil ecological and soil hydraulic properties. Geoderma 332, 10–19.

Schlüter, S., Albrecht, L., Schwärzel, K., Kreiselmeier, J., 2020. Long-term effects of conventional tillage and no-tillage on saturated and near-saturated hydraulic conductivity – can their prediction be improved by pore metrics obtained with X-ray CT? Geoderma 361, 114082.

Schwenk, A., Jarvis, N., Larsbo, M., Koestel, J., 2023. Three-dimensional imaging of macropore flow. Geoderma 440, 116721.

Šimůnek, J., Jarvis, N., van Genuchten, M.T., Gärdenäs, A., 2003. Review and comparison of models for describing nonequilibrium and preferential flow and transport in the vadose zone. J. Hydrol. 272, 14–35.

Soto-Gómez, D., Vázquez Juíz, L., Pérez-Rodríguez, P., López-Periago, J., Paradelo, M., Koestel, J., 2020. Percolation theory applied to soil tomography. Geoderma 357, 113959.

Wildenschild, D., Hopmans, J., Simunek, J., 2001. Flow rate dependence of soil hydraulic characteristics. Soil Sci. Soc. Am. J. 65, 35–48.